Asociación Argentina
de Mecánica Computacional

Mecánica Computacional Vol XXVIII, págs. 1131-1148 (artículo completo)
Cristian García Bauza, Pablo Lotito, Lisandro Parente, Marcelo Vénere (Eds.)
Tandil, Argentina, 3-6 Noviembre 2009

IMPROVED INTERPOLANTS FOR DISCONTINUOUS PRESSURES

F. S. Sousa[a], R. F. Ausas[b] and G. C. Buscaglia[a]

[a]*Instituto de Ciências Matemáticas e de Computação (ICMC), Universidade de São Paulo (USP), Av. Trabalhador São-Carlense 400, 13560-970, São Carlos, Brazil, fsimeoni@icmc.usp.br, gustavo.buscaglia@icmc.usp.br, http://www.lcad.icmc.usp.br*

[b]*Centro Atómico Bariloche e Instituto Balseiro, Av. Bustillo 9500, 8400 Bariloche, Argentina, rfausas@gmail.com, http://cab.cnea.gov.ar*

Keywords: Finite elements, interface, interpolation, discontinuous pressure, surface tension

Abstract. We consider 2D incompressible Stokes flow with an internal interface at which the pressure is discontinuous, as happens for example in problems involving surface tension. We assume that the internal interface is a line that does not coincide with the mesh edges, and propose a piecewise-linear pressure space with improved interpolation properties. The functions in the proposed space are discontinuous only at the interface, coinciding with standard P_1 functions away from it. Further, the degrees of freedom are exactly the same as those of the standard, conforming P_1 space, making it straightforward to incorporate the proposed method in existing codes. We implement the well-known mini-element and show that switching to the proposed pressure space at the elements cut by the interface significantly reduces the error in both pressure and velocity.

1 INTRODUCTION

Though much progress has been made over the last years in the field of finite-element-based computational fluid mechanics, the accurate simulation of flows with significant surface tension effects remains a challenge. This is a consequence of two main difficulties that are inherent to such flows:

(i) The surface tension force F_Γ is a surface Dirac distribution over the interface Γ, proportional to the curvature of Γ. The singularity of the force, together with its dependence of second derivatives of the interface shape, renders it difficult to approximate.

(ii) Some of the flow variables, most importantly the pressure, are discontinuous across Γ. This leads to suboptimal interpolation accuracy whenever the finite element interpolants are continuous across Γ.

In a recent careful study, Gross and Reusken (2007a,b) (see also Reusken (2008)), have shown that both of the aforementioned difficulties need to be specifically addressed or otherwise the convergence is poor (of order $h^{\frac{1}{2}}$). In this article the attention is focused in difficulty (ii), for which Gross and Reusken propose to adopt an XFEM (Belytschko et al., 2001) enrichment of the pressure space, incorporating functions that are discontinuous at Γ, as had been also proposed by Minev et al. (2003). With this modification, they are able to get improved convergence behavior, at the expense of the well-known pitfalls of the XFEM methodology: The ill-conditioning of the system matrix due to approximate linear dependence of the basis, and the introduction of new unknowns that depend on the location of the interface, thus requiring the code to completely rebuild the linear system structure for each interface location.

Similar considerations have been made recently by Ganesan et al. (2007). They compare mixed finite elements with continuous and discontinuous approximations for the pressure, and end up recommending the use of meshes that follow the interface together with discontinuous pressure interpolants. Clearly, this is the only combination of classical finite elements that yields a pressure space that is discontinuous at Γ, which is the key to properly tackle difficulty (ii) above. However, in a dynamic simulation it is cumbersome and sometimes impossible to maintain the mesh aligned with the interface, so that other remedies must be sought.

In this article we introduce a novel pressure space which accommodates discontinuities at the (given) interface Γ, which is approximated by piecewise-linear segments in 2D and piecewise-planar facets in 3D. The proposed space is nothing but the classical conforming P_1 space, locally modified at those elements that are cut by the interface (which will be denoted as *interface elements*). The modification is local, computed element-by-element, and it does not introduce any additional degrees of freedom. It is thus extremely easy to incorporate the proposed space into existing codes. Further, the only discontinuities take place at Γ, so that no special treatment is needed at other interfaces (such as element-to-element interfaces, for example, as happens with Discontinuous Galerkin methods).

The proposed pressure space will be introduced in the framework of the (two-dimensional for simplicity) problem

$$-\mu\nabla^2 u + \nabla p = F_\Gamma \quad \text{in } \Omega \tag{1}$$

$$\nabla \cdot u = 0 \quad \text{in } \Omega \tag{2}$$

$$u = 0 \quad \text{on } \partial\Omega \tag{3}$$

where $F_\Gamma = f\,\delta_\Gamma\,\mathbf{n}$, with f a given function, δ_Γ the Dirac delta distribution on the line Γ, and $\mathbf{n}$ its normal. The singular force F_Γ acts in fact as a jump condition on the normal stress across Γ,

namely,

$$\left[\!\left[-p + 2\mu\frac{\partial u_n}{\partial n}\right]\!\right] = f, \tag{4}$$

whereas both the velocity and the tangential stress remain continuous. In fact, in this constant-viscosity case the velocity gradient exhibits no jump across Γ (Gross and Reusken, 2007a), so that (4) reduces to $[\![p]\!] = -f$. Notice that this simplified model also represents the so-called *actuator-disk model* that is very popular in the analysis of rotors (propellers, wind turbines, etc.) (Meyer and Kröger, 2001; Tahara et al., 2006; Carrica et al., 2008; Leclerc and Masson, 2005).

Denoting by $V = H_0^1(\Omega) \times H_0^1(\Omega)$ and $Q = L^2(\Omega)/\mathbb{R}$, the variational formulation that corresponds to (1)-(3) reads: "Find $(u, p) \in V \times Q$ such that

$$\int_\Omega \left[\mu(\nabla u + \nabla^T u) : \nabla v - p\,\nabla\cdot v + q\,\nabla\cdot u\right]\, d\Omega = \int_\Gamma f\,\mathbf{n}\cdot v\, d\Gamma \tag{5}$$

for all $(v, q) \in V \times Q$". The bilinear and linear forms associated to the variational formulation will be denoted by $B(\cdot,\cdot)$ and $L(\cdot)$, so that (5) can be rewritten as

$$B((u, p), (v, q)) = L(v, q). \tag{6}$$

Under reasonable regularity assumptions on Γ and f this problem admits a unique solution, since it is only necessary that L be a bounded linear functional. The finite element discretization of (5) is briefly recalled in Section 2, together with the description of the proposed pressure space. Section 3 contains several numerical experiments that assess the advantages of the proposed space with respect to classical spaces. Some conclusions are finally drawn in Section 4.

2 FINITE ELEMENT APPROXIMATION

2.1 Galerkin mini-element formulation

In the Galerkin formulation, the exact variational formulation is restricted to the space $V_h \times Q_h$, where $V_h \subset V$ and $Q_h \subset Q$ are the approximation spaces for velocity and pressure, respectively. The discrete formulation thus reads "Find $(u_h, p_h) \in V_h \times Q_h$ such that

$$B((u_h, p_h), (v_h, q_h)) = L(v_h, q_h) \tag{7}$$

for all $(v_h, q_h) \in V_h \times Q_h$". As is well-known, for this formulation to be well-posed and convergent it is sufficient that the Babuška-Brezzi stability condition (Babuška, 1973; Brezzi, 1974) be satisfied:

$$\inf_{q_h \in Q_h} \sup_{v_h \in V_h} \frac{\int_\Omega q_h\,\nabla\cdot v_h\, d\Omega}{\|q_h\|_Q\,\|v_h\|_V} \geq \beta > 0 \tag{8}$$

with β a mesh-independent constant.

The pressure and velocity spaces that correspond to the so-called mini-element (Arnold et al., 1984) are, for a finite element mesh $\mathcal{T}_h$:

$$Q_h = Q_h^1 := \{q_h \in Q \cap \mathcal{C}^0(\Omega),\ q_h|_K \in P_1(K),\ \forall\, K \in \mathcal{T}_h\} \tag{9}$$

$$V_h = V_h^{\text{mini}} := \{v_h \in V,\ v_h|_K \in (P_1(K) \oplus \text{span}(b_K))^2,\ \forall\, K \in \mathcal{T}_h\} \tag{10}$$

where b_K is the cubic bubble function that vanishes on all three edges of K. Notice that the pressure space is nothing but the usual continuous P_1 space, while the space for each velocity

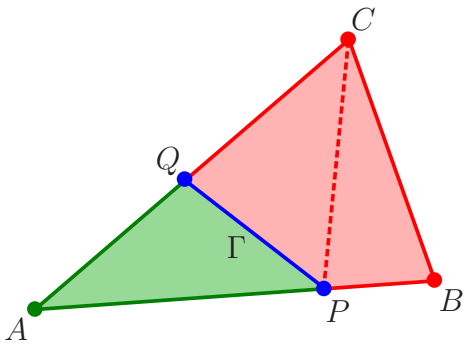

Figure 1: Partition of a single finite element into subelements following the interface PQ.

component has been enriched by the bubble functions so as to satisfy the stability condition. Being stable, this element satisfies the a priori estimate

$$\|u-u_h\|_V + \|p-p_h\|_Q \leq C \left(\inf_{w_h \in V_h} \|u-w_h\|_V + \inf_{r_h \in Q_h} \|p-r_h\|_Q \right) \tag{11}$$

where C does not depend on the mesh size h. In the case of a smooth solution, there exists a constant c such that $\inf_{w_h \in V_h} \|u-w_h\|_V \leq c\,h\,|u|_{H^2(\Omega)}$ whereas $\inf_{r_h \in Q_h} \|p-r_h\|_Q \leq c\,h^2\,|p|_{H^2(\Omega)}$. In the case of non-smooth solutions involving pressure jumps, however, the latter interpolation estimate deteriorates significantly (Gross and Reusken, 2007a), to

$$\inf_{r_h \in Q_h} \|p-r_h\|_Q \leq C \left(h^{\frac{1}{2}} \|[\![p]\!]\|_{L^\infty(\Gamma)} + h^2 \|p\|_{H^2(\Omega\setminus\Gamma)} \right)$$

This approximation error of order $h^{\frac{1}{2}}$ is a direct consequence of the pressure interpolants being continuous *across* Γ, so that switching to discontinuous-pressure elements does not cure it, unless the mesh follows the interface.

2.2 A discontinuous pressure space with the same unknowns

The proposed variant of the mini-element combines the velocity space V_h^{mini} (Eq. 10) with a new pressure space Q_h^Γ discussed below, without any modification of the Galerkin formulation (7).

2.2.1 The finite element interpolant

Let us now propose a different finite element space, denoted by Q_h^Γ, which has the same unknowns as the conforming P_1 space Q_h^1 but admits discontinuities across Γ. For all elements not cut by Γ standard P_1 interpolants are chosen. The only modifications appear in interface elements.

Consider the triangle ABC, which is cut by Γ into subtriangle APQ and subquadrilateral $BCQP$ (see Fig. 1). We assume for simplicity that, locally, Γ is approximated by linear segments (this would probably add an additional error of order h^2, much smaller than the other errors involved). Let p_A, p_B, p_C denote the nodal values of the discrete pressure p_h, to be interpolated in the triangle ABC.

Let us arbitrarily denote the triangle APQ the "green" side of Γ and quadrilateral $BCQP$ the "red" side. For the approximation to be discontinuous, the function p_h on the green side needs to be solely determined by the only green node, i.e., A. Similarly, p_h on the red side

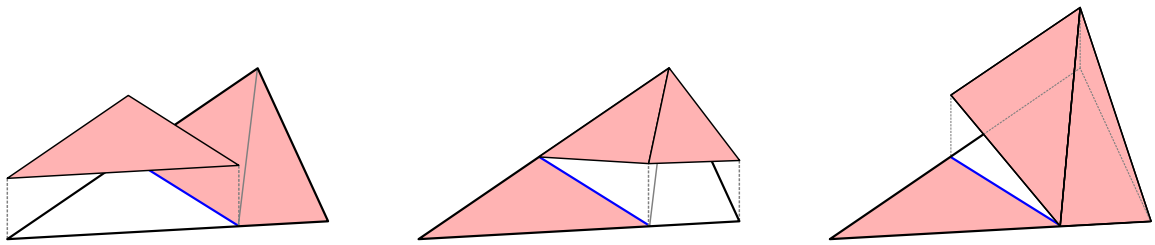

(a) (b) (c)

Figure 2: Basis functions for the new finite element space inside an element crossed by the interface: (a) N_A, (b) N_B and (c) N_C.

must depend on just p_B and p_C. To accomplish this, we simply "carry" the value at each node towards the intersection of any edge emanating from it with the interface.

In this way, on the green side of Γ, the values at P and Q will be p_A, and thus p_h will be constant:

$$p_h|_{APQ} = p_A$$

On the red side, the value at P will be p_B and the value at Q will be p_C. One can here choose either to adopt a Q_1 interpolation in $BCQP$ from these nodal values, or subdivide the quadrilateral into two triangles, BCP and CQP. In any case, since the nodal values are given, the interpolation is immediate. For the red triangle CQP, for example, p_h will be the linear function that takes the value p_C at vertex C, the value p_C at vertex Q, and the value p_B at vertex P. Notice that this interpolation leads to p_h being discontinuous *only at* Γ, since the function p_h restricted to any edge of the triangle is uniquely determined by the values at the nodes lying at the endpoints of that edge.

As a consequence of carrying the nodal values towards the intersection of each edge with the interface, the space Q_h^Γ consists of functions with locally an oblique derivative (in the direction of the edge that happens to cross Γ at each point) equal to zero. The interpolation error $\|p - I_h p\|_Q$ is thus expected to be of order $h^{\frac{3}{2}}$ for arbitrary $p \in W^{1,\infty}(\Omega \setminus \Gamma)$.

Remark: It could be interesting to modify the proposed space in such a way as to obtain an interpolation order of h^2 for functions with any derivative at Γ. A suitable way to do this would be by extrapolation along the edge using some recovered gradient at the nodes. This is an operation that cannot be carried out at the element level alone, and has not been explored in this work.

Remark: Some modifications are needed if the interface Γ ends within the domain (i.e., a *cracked* domain). Consider that the interface ends at some point T that lies between P and Q, so that the segment TQ is not contained in Γ. In this case the value of p_h at Q is computed by linearly interpolating the values p_A and p_C along the edge AC. The treatment of the intersection point P is as before, so that the interpolant is continuous at Q and discontinuous at P.

The extension of the proposed methodology to three dimensions follows the lines described above. For completeness, the basis functions are given explicitly for the different possible cases in the paragraphs that follow.

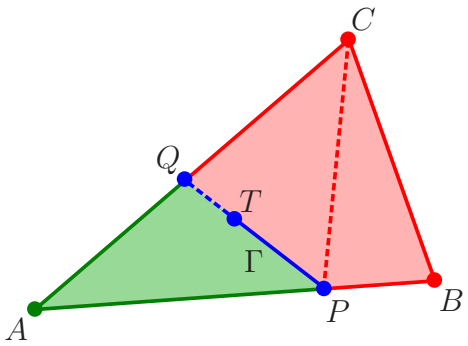

Figure 3: Endpoint T of the interface Γ inside the element ABC.

2.2.2 Two-dimensional case: Standard interface element

Consider as before the triangle ABC, which is cut by Γ into the "green" subtriangle APQ and the "red" subtriangles BCP and CQP. The basis functions N_A, N_B and N_C are defined to be piecewise affine inside each of these subtriangles. It only remains to define their values at the vertices of the subtriangles, i.e., at the points A, B, C, P and Q. However, since they are discontinuous at Γ, two values are given at points P and Q. The values on the green side will be assigned a "plus" sign, while those on the red side a "minus" sign. The values at the vertices are:

$$N_A(A) = 1 \quad N_B(A) = 0 \quad N_C(A) = 0 \tag{12}$$
$$N_A(B) = 0 \quad N_B(B) = 1 \quad N_C(B) = 0 \tag{13}$$
$$N_A(C) = 0 \quad N_B(C) = 0 \quad N_C(C) = 1 \tag{14}$$
$$N_A(P^+) = 1 \quad N_B(P^+) = 0 \quad N_C(P^+) = 0 \tag{15}$$
$$N_A(P^-) = 0 \quad N_B(P^-) = 1 \quad N_C(P^-) = 0 \tag{16}$$
$$N_A(Q^+) = 1 \quad N_B(Q^+) = 0 \quad N_C(Q^+) = 0 \tag{17}$$
$$N_A(Q^-) = 0 \quad N_B(Q^-) = 0 \quad N_C(Q^-) = 1 \tag{18}$$

Notice that these functions satisfy several useful properties: (i) They form a nodal basis, in the sense that they take the value one at their corresponding node and zero at the other nodes; (ii) their sum equals the constant function equal to one in K; (iii) their extreme values (zero and one) take place at the nodes. A picture of the interpolation functions for this case can be seen on Fig. 2.

Remark: Though unlikely in practical cases, it could happen that Γ passes exactly through a vertex. This is a degenerate case in which one of the subtriangles becomes a needle of vanishingly small volume.

2.2.3 Two-dimensional case: Element containing an endpoint of the interface

In the case that Γ has an endpoint at element K, special basis functions are needed. Consider P to be the last edge-interface intersection point, and T to be the interface endpoint (see Figure 3). The point Q is defined as the intersection of the line PT with the edge AC. The difference with the previous case is that now the functions need to be continuous at point Q.

For this purpose, let g be an affine function defined on the edge AC such that $g(A) = 1$ and $g(C) = 0$ (in other words, g is the restriction to edge AC of the P_1 basis function corresponding

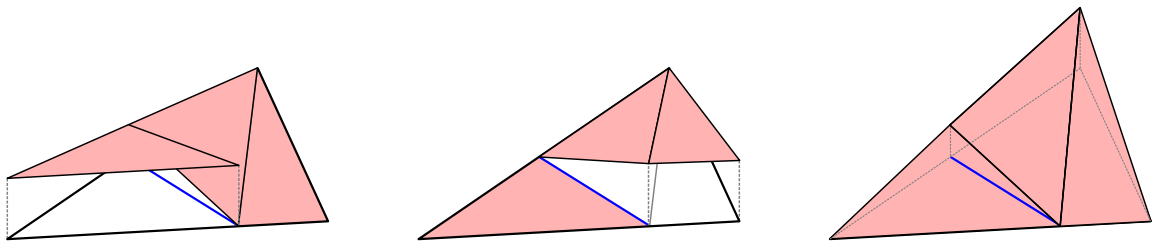

(a) (b) (c)

Figure 4: Basis functions for the new finite element space inside an element containing an endpoint of the interface: (a) N_A, (b) N_B and (c) N_C.

to node A). The values of N_A, N_B and N_C at points A, B, C, P^+ and P^- are as in (12)-(16). At point Q the functions are continuous, with values

$$N_A(Q) = g(Q), \qquad N_B(Q) = 0, \qquad N_C(Q) = 1 - g(Q) \tag{19}$$

Properties (*i*)-(*iii*) above are also satisfied by this basis. An illustration of these functions can be seen on Fig. 4.

2.2.4 Three-dimensional case: Standard interface element

Consider that the element K cut by the interface is the tetrahedron $ABCD$ as shown in Fig. 5, of which either three (case (a)) or four (case (b)) edges are cut by Γ.

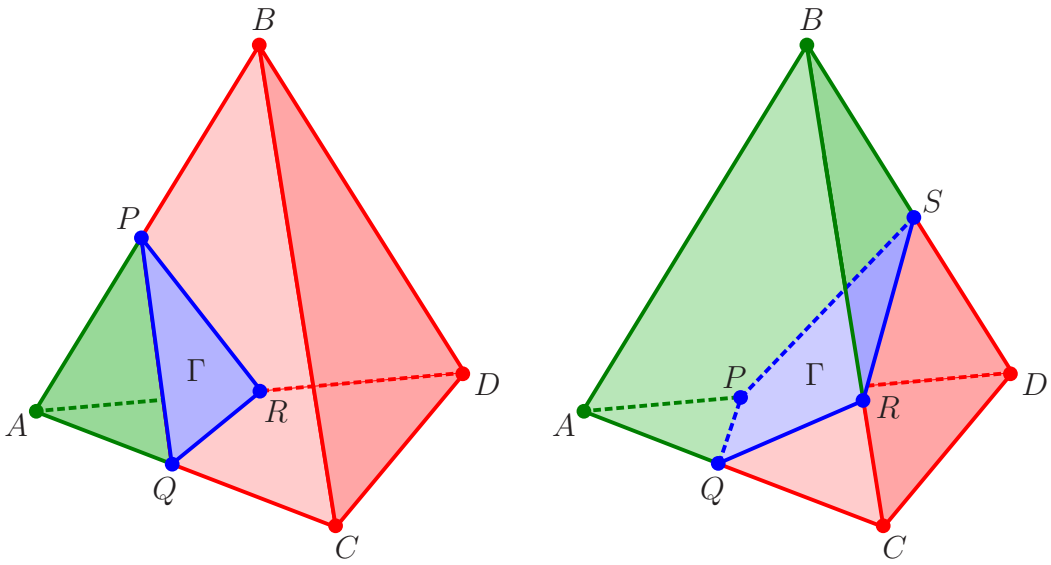

Figure 5: Partition of a tetrahedron following interface Γ: (a) Interface crossing three edges; (b) Interface crossing four edges.

In case (a), there appear three intersection points P, Q and R (see Fig. 5(a)), at which the nodal functions N_A, N_B, N_C and N_D are bivaluated. As in the two-dimensional case, the plus and minus values at the intersection points correspond to the "green" and "red" sides of the

interface. Carrying the values to the interface as explained, the values of the basis functions at the vertices and intersection points are:

$$N_A(A)=1, \quad N_B(A)=0, \quad N_C(A)=0, \quad N_D(A)=0 \tag{20}$$
$$N_A(B)=0, \quad N_B(B)=1, \quad N_C(B)=0, \quad N_D(B)=0 \tag{21}$$
$$N_A(C)=0, \quad N_B(C)=0, \quad N_C(C)=1, \quad N_D(C)=0 \tag{22}$$
$$N_A(D)=0, \quad N_B(D)=0, \quad N_C(D)=0, \quad N_D(D)=1 \tag{23}$$
$$N_A(P^+)=1, \quad N_B(P^+)=0, \quad N_C(P^+)=0, \quad N_D(P^+)=0 \tag{24}$$
$$N_A(P^-)=0, \quad N_B(P^-)=1, \quad N_C(P^-)=0, \quad N_D(P^-)=0 \tag{25}$$
$$N_A(Q^+)=1, \quad N_B(Q^+)=0, \quad N_C(Q^+)=0, \quad N_D(Q^+)=0 \tag{26}$$
$$N_A(Q^-)=0, \quad N_B(Q^-)=0, \quad N_C(Q^-)=1, \quad N_D(Q^-)=0 \tag{27}$$
$$N_A(R^+)=1, \quad N_B(R^+)=0, \quad N_C(R^+)=0, \quad N_D(R^+)=0 \tag{28}$$
$$N_A(R^-)=0, \quad N_B(R^-)=0, \quad N_C(R^-)=0, \quad N_D(R^-)=1 \tag{29}$$

The truncated tetrahedron $BCDPQR$ is divided into subtetrahedra and from the values at the vertices given above the basis functions are obtained by affine interpolation over each subtetrahedron. Satisfaction of 3D analogs of properties (*i*)-(*iii*) is straightforward. In this case, for the resulting interpolant not to be discontinuous at the faces (outside Γ) the neighbor element be subdivided in a compatible way. For face ABC, for example, continuity of N_B and N_C is only obtained if both elements sharing this face divide the quadrilateral $BCPQ$ by the same diagonal.

In case (b) there appear four intersection points, namely P, Q, R and S (see Fig. 5(b)). The values of the basis functions at A, B, C and D are obviously the same as in (20)-(23). The values at the intersection points follow the same procedure as before, yielding

$$N_A(P^+)=1, \quad N_B(P^+)=0, \quad N_C(P^+)=0, \quad N_D(P^+)=0 \tag{30}$$
$$N_A(P^-)=0, \quad N_B(P^-)=0, \quad N_C(P^-)=1, \quad N_D(P^-)=0 \tag{31}$$
$$N_A(Q^+)=1, \quad N_B(Q^+)=0, \quad N_C(Q^+)=0, \quad N_D(Q^+)=0 \tag{32}$$
$$N_A(Q^-)=0, \quad N_B(Q^-)=0, \quad N_C(Q^-)=0, \quad N_D(Q^-)=1 \tag{33}$$
$$N_A(R^+)=0, \quad N_B(R^+)=1, \quad N_C(R^+)=0, \quad N_D(R^+)=0 \tag{34}$$
$$N_A(R^-)=0, \quad N_B(R^-)=0, \quad N_C(R^-)=1, \quad N_D(R^-)=0 \tag{35}$$
$$N_A(S^+)=0, \quad N_B(S^+)=1, \quad N_C(S^+)=0, \quad N_D(S^+)=0 \tag{36}$$
$$N_A(S^-)=0, \quad N_B(S^-)=0, \quad N_C(S^-)=0, \quad N_D(S^-)=1 \tag{37}$$

Properties (*i*)-(*iii*) are easily seen to hold, while continuity across the faces again depends on the compatibility of the subdivisions between neighboring elements.

2.2.5 Three-dimensional case: Interface with boundary

If the interface Γ has a boundary $\partial\Gamma$ within the domain, the basis functions need to be modified in much the same way as in the two-dimensional case. Let K be an element cut by the surface Γ and such that $\partial\Gamma \cap K \neq \emptyset$. We assume that $\Gamma \cap K$ is a planar polygon and thus the intersection of this plane with the edges of K defines the points P, Q, R and, in a case-(b) situation, S, as before.

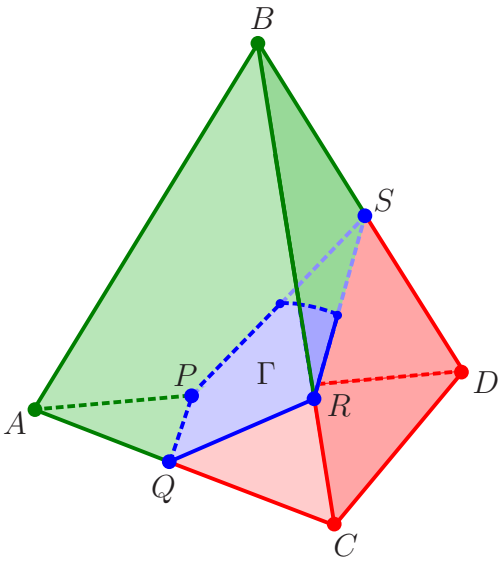

Figure 6: Partition of a tetrahedron K where $\partial\Gamma \cap K \neq \emptyset$. Point S is obtained by intersecting plane PQR with edge BD.

Consider for example that the intersection is as shown in Fig. 6, so that the subdivision corresponds to case (b). Notice, however, that the edge BD is not crossed by the interface, so that the basis functions must be continuous along this edge and thus, in particular, at point S. Proceeding as in the two-dimensional case, we assign to S a unique value provided by the linear interpolation between nodes B and D. This procedure is adopted for all intersection points falling outside Γ. Properties (*i*)-(*iii*) are easily seen to hold, as well as continuity of the basis functions across the faces (again depending on a compatible choice of diagonals for quadrilaterals).

3 NUMERICAL EXPERIMENTS

3.1 Interpolation properties of the space Q_h^Γ

We first assess purely the interpolation properties of Q_h^Γ. For this purpose we perform tests similar to those conducted by Reusken (Reusken, 2008). Let $\Omega = (-\frac{\pi}{2}, \frac{\pi}{2}) \times (-\frac{\pi}{2}, \frac{\pi}{2})$ and let $\Gamma = \{(x, y) \in \Omega \,|\, x = 0\,,\; y > 0\}$. Let p be the function

$$p(x,y) = \begin{cases} e^{-x}\,\sin^2(y) & \text{if } (x > 0 \text{ and } y > 0) \\ 0 & \text{otherwise} \end{cases} . \tag{38}$$

Notice that Γ is a "crack" in the domain, and that p is discontinuous across Γ.

For an arbitrary triangulation $\mathcal{T}_h$, the interface Γ is approximated by Γ_h, where Γ_h is composed of all the linear segments joining, in each triangle K totally cut by Γ, the two intersections of Γ with the edges of K, plus the triangle containing the endpoint of Γ. Notice that this makes, in this case, that Γ_h is slightly bigger than Γ, but the error introduced by this procedure is much smaller than interpolation errors.

The interpolant $\mathcal{I}_h p$ of p is now defined as the unique element of $Q_h^{\Gamma_h}$ that coincides with p at all the vertices of $\mathcal{T}_h$.

A sequence of unstructured meshes was built, of which the first one is shown in Fig. 7. To this mesh, which consists of 326 triangles, we assign a mesh size of $h = 0.2$. The following meshes in the sequence are built by successively dividing each of the triangles of the previous

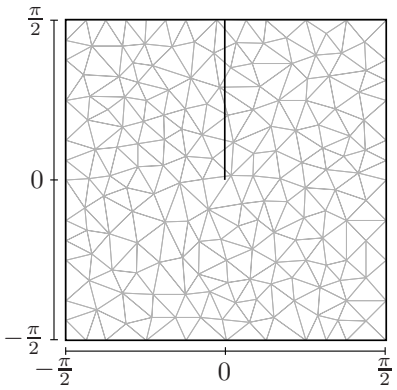

Figure 7: First mesh used in the interpolation test, with 326 elements. The interface Γ is a line from (0,0) to (0,$\frac{\pi}{2}$).

h	Q_h^1	Q_h^Γ
2.0×10^{-1}	1.332321×10^{-1}	4.166473×10^{-2}
1.0×10^{-1}	1.120209×10^{-1}	1.593032×10^{-2}
5.0×10^{-2}	7.209146×10^{-2}	4.456308×10^{-3}
2.5×10^{-2}	5.126917×10^{-2}	1.606452×10^{-3}
1.25×10^{-2}	3.607274×10^{-2}	5.286712×10^{-4}
6.25×10^{-3}	2.565891×10^{-2}	2.010631×10^{-4}
3.125×10^{-3}	1.786352×10^{-2}	6.614845×10^{-5}

Table 1: Error $\|p - \mathcal{I}p\|_{L^2(\Omega)}$ for the standard Q_h^1 space, compared to the new pressure space Q_h^Γ.

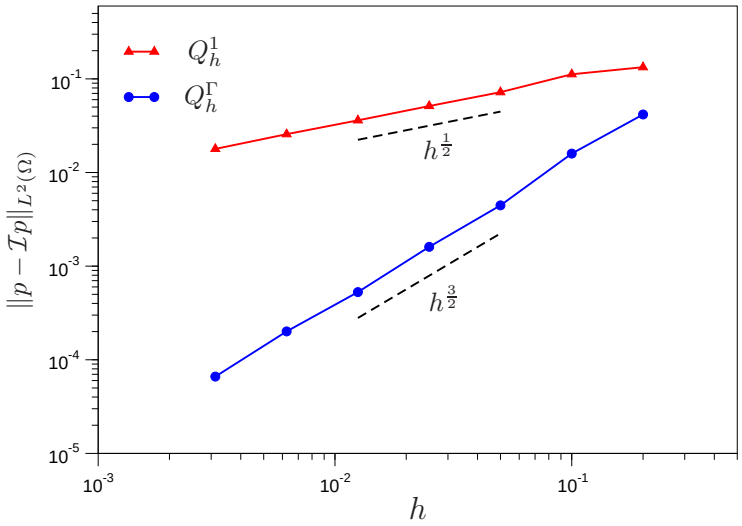

Figure 8: Convergence rate of the error in L^2-norm for the interpolated function $p(x, y)$ using standard Q_h^1 and the new pressure space Q_h^Γ.

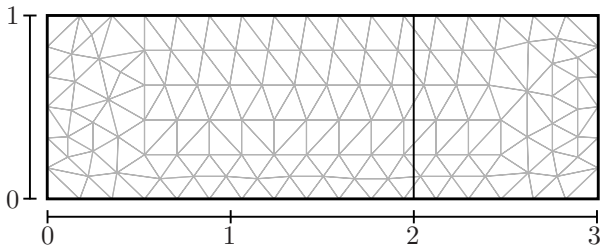

Figure 9: Mesh with 220 elements, $h = 0.176$, for the Couette convergence test.

mesh into four equal triangles, leading to meshes with $h = 0.1$, $h = 0.05$ and so forth, until the finest mesh with $h = 3.125 \times 10^{-3}$.

We measured the error of $p - \mathcal{I}_h p$ in the $L^2(\Omega)$-norm. The results are shown in Table 1, in which we also include the interpolation error of the P_1-conforming interpolant for comparison (Q_h^1). Figure 8 displays the convergence rate of the order of $h^{\frac{3}{2}}$ for both cases.

3.2 Couette flow

In this experiment we consider the domain $[0, L] \times [0, H]$, with periodic boundary conditions in the x_1-direction. The velocity is set to zero at the top and bottom boundaries

$$u(x_1, x_2 = 0) = u(x_1, x_2 = H) = 0$$

and the interface Γ is a straight vertical line $x_1 = a$, on which a constant unit normal force $f = 1$ is imposed. The exact solution for this problem is

$$u_1(x_1, x_2) = \frac{1}{2\mu L}\, x_2\,(H - x_2) \tag{39}$$

$$u_2(x_1, x_2) = 0 \tag{40}$$

$$p(x_1, x_2) = -\frac{1}{L} x_1 + \mathcal{H}(x_1 - a) \tag{41}$$

where $\mathcal{H}(x_1 - a) = 1$ if $x_1 > a$ and zero otherwise, and the indeterminacy of the pressure was removed by imposing $p(0, 0) = 0$ instead of setting the average to zero, for simplicity.

This problem, with $L = 3$, $H = 1$, $\mu = 1$ and $a = 2$ was discretized with the mini-element, using the classical P_1-conforming pressure space (denoted by Q_h^1 above) and the new space Q_h^Γ.

As in the previous section, a sequence of unstructured meshes was built, of which the first one is shown in Fig. 9. To this mesh, which consists of 220 triangles, we assign a mesh size of $h = 0.176$. The following meshes in the sequence are built by subdivision. We measure the velocity error in the $H^1(\Omega)$-norm and the pressure error in the $L^2(\Omega)$-norm for both methods as functions of h. The results of the convergence analysis are displayed in Fig. 10. The experimental orders of convergence are

$$\|u - u_h\|_{H^1(\Omega)} = \mathcal{O}(h^{\frac{1}{2}}), \qquad \|p - p_h\|_{L^2(\Omega)} = \mathcal{O}(h^{\frac{1}{2}})$$

for the standard Q_h^1 space; and

$$\|u - u_h\|_{H^1(\Omega)} = \mathcal{O}(h), \qquad \|p - p_h\|_{L^2(\Omega)} = \mathcal{O}(h)$$

for the proposed method. The optimal convergence of smooth problems is thus recovered with the proposed modification of the pressure space.

The pressure fields corresponding to the classical mini-element is compared to that obtained with the proposed method in Fig. 11. As is clear from the figure, the improved pressure space exhibits significantly smaller pressure oscillations near the interface than the mini-element.

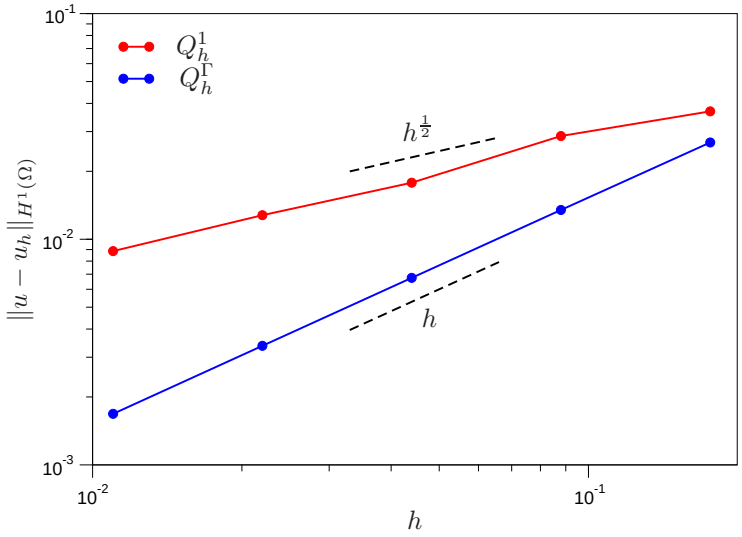

(a)

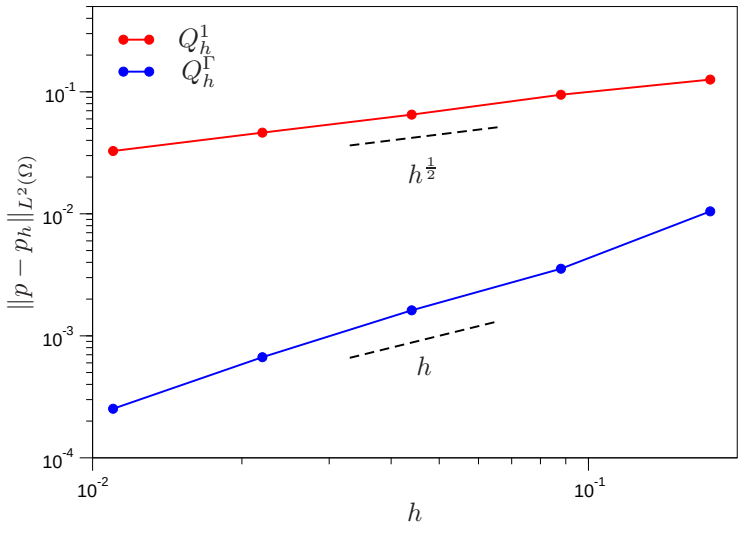

(b)

Figure 10: Error norms for the velocity (a) and pressure (b), showing the convergence rates for the Couette flow.

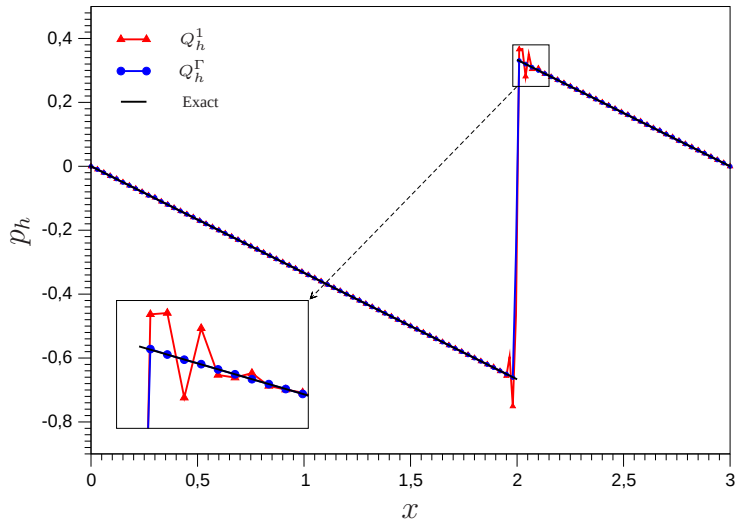

Figure 11: Computed pressure using the stable formulation (mini-element), with standard and new pressure space.

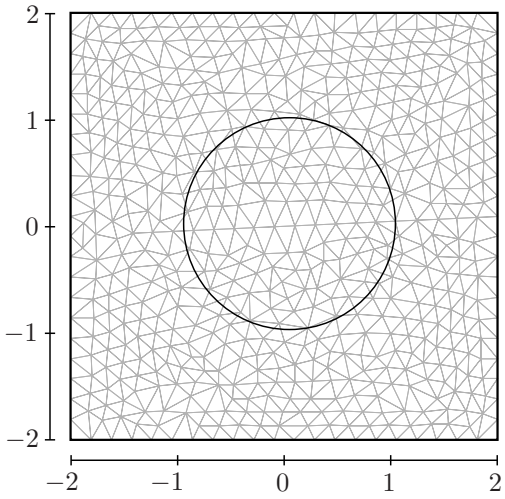

Figure 12: Mesh for the static bubble convergence study, with 1104 elements and $h = 0.2$.

3.3 Static two-dimensional bubble

The second example we report here concerns a 2D static bubble. In this case the interface Γ is the circle of radius R centered at the origin. On Γ, a constant (inwards) normal force is imposed, $f = \frac{\sigma}{R}$, where σ represents the surface tension. Setting the pressure outside the bubble arbitrarily to zero, the exact pressure inside the bubble equals $\frac{\sigma}{R}$. The exact velocity vanishes everywhere.

In this example we approximate Γ by Γ_h, which consists of straight segments inside each element that join the intersections of Γ with the element edges (i.e., the points P and Q are joined by a straight segment). With Γ_h fixed, we impose the surface tension force by

$$F_\Gamma = -\frac{\sigma}{R}\,\delta_{\Gamma_h}\,\mathbf{e}_r \tag{42}$$

where $\mathbf{e}_r$ is the radial unit vector, leading to

$$L(v_h, q_h) = -\frac{\sigma}{R}\int_{\Gamma_h} \mathbf{e}_r \cdot v_h \, d\Gamma \tag{43}$$

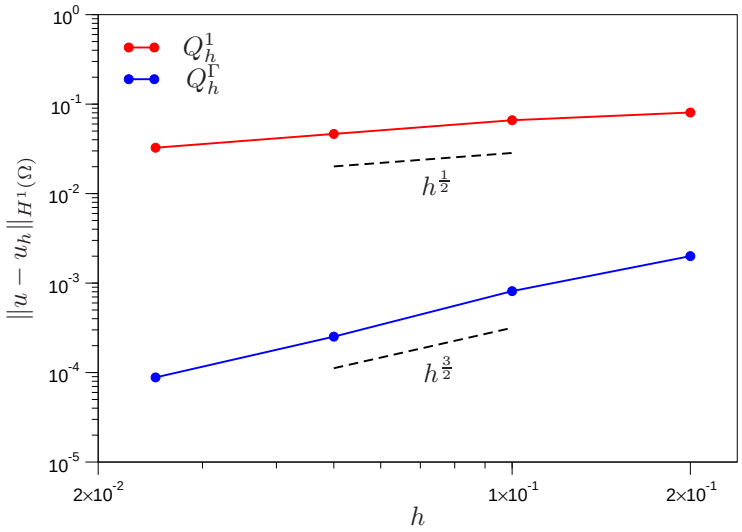

(a)

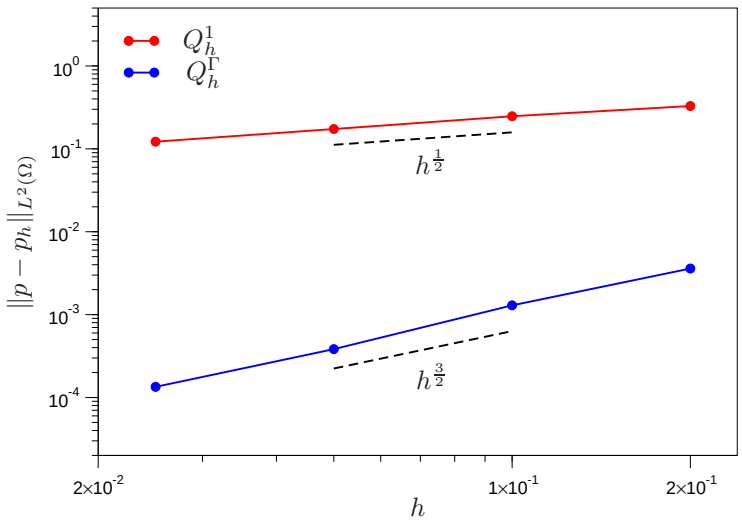

(b)

Figure 13: Error norms for the velocity (a) and pressure (b), showing the convergence rates for the static bubble.

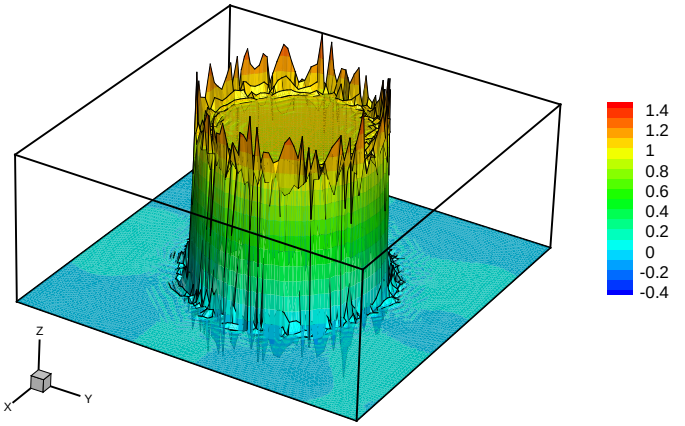

(a)

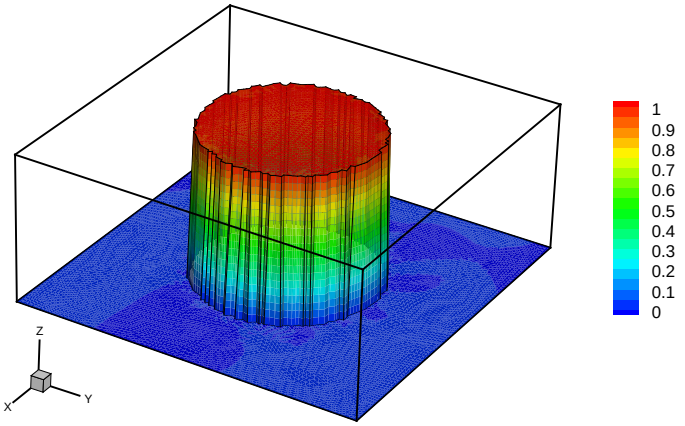

(b)

Figure 14: Pressure field for the mini-element with direct forcing, obtained with $h = 0.05$: (a) Q_h^1; (b) Q_h^Γ.

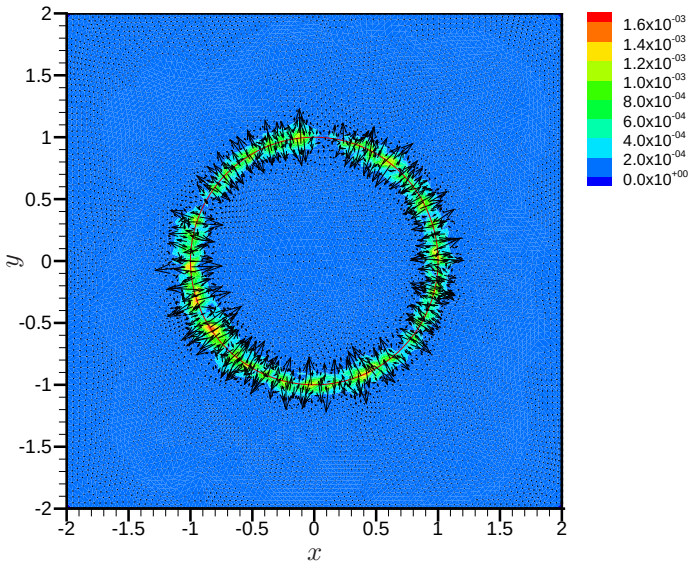

(a)

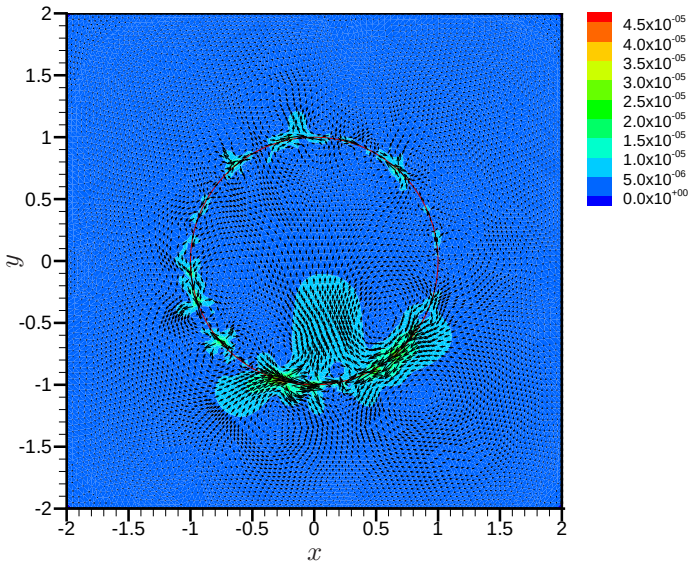

(b)

Figure 15: Spurious velocities for the mini-element with direct forcing, obtained with $h = 0.05$: (a) Q_h^1; (b) Q_h^Γ.

For the numerical tests we chose $R = \mu = \sigma = 1$, and the domain was set to $\Omega = (-2, 2) \times (-2, 2)$. The velocity is set to zero on $\partial\Omega$, and the pressure at the left bottom corner of the domain is set to zero to fully determine the pressure. A mesh refinement study was conducted in the same way as in the previous examples, starting with the mesh shown in Fig. 12, to which we assign $h = 0.2$. Logarithmic plots of the velocity and pressure errors are shown in Fig. 13. Clearly, the method converges with order $\mathcal{O}(h^{\frac{1}{2}})$ if the standard pressure space Q_h^1 is used, while switching to Q_h^Γ improves the order to $\mathcal{O}(h^{\frac{3}{2}})$. The obtained pressure and velocity fields on the mesh with $h = 0.05$, which consists of 14900 elements, are shown in Figs. 14 and 15. The improvements brought by the proposed method are evident. The parasitic velocities obtained with this formulation have a maximum modulus of 1.6×10^{-3} when the P_1 space is used for pressure, whereas with the proposed space this value is much smaller (4.5×10^{-5}).

4 CONCLUSIONS

A new finite element space Q_h^Γ has been proposed, which has the same unknowns as the P_1-conforming space but consists of functions that are discontinuous across a given interface Γ, assumed not aligned with the mesh. The proposed space is much simpler than the one proposed by Gross and Reusken (2007a), which is based on XFEM enrichment, and also to the one proposed by Fries and Belytschko (2006), which avoids introducing additional unknowns by switching to a moving-least-squares approximation in the vicinity of Γ.

Through numerical tests it was shown that the $L^2(\Omega)$-interpolation accuracy of Q_h^Γ for functions that are smooth outside Γ is $\mathcal{O}(h^{\frac{3}{2}})$. This is a significant improvement with respect to the accuracy of continuous spaces of any polynomial degree, which is $\mathcal{O}(h^{\frac{1}{2}})$

An interpolation accuracy of $\mathcal{O}(h^{\frac{3}{2}})$ in the $L^2(\Omega)$-norm is suboptimal for piecewise linear elements. However, the a priori estimate (11) implies that the space Q_h^Γ, when taken as pressure space, will *not* limit the accuracy of a (Navier-)Stokes calculation in the mini-element approximation (neither in equal-order velocity-pressure approximations). In fact, in both cases the global accuracy is limited by the $H^1(\Omega)$-accuracy of the velocity space, which is $\mathcal{O}(h)$.

The proposed space is easy to implement, requiring just local operations at the element level to incorporate the improved pressure interpolation. Several tests were reported which illustrate the improved behavior of both velocity and pressure when the elements cut by the interface are treated with the proposed pressure interpolants.

ACKNOWLEDGMENTS: The authors acknowledge partial support from FAPESP (Brasil), CNPq (Brasil), CNEA (Argentina) and CONICET (Argentina).

REFERENCES

Arnold D., Brezzi F., and Fortin M. A stable finite element for the stokes equations. *Calcolo*, 21:337–344, 1984.

Babuška I. The finite element method with Lagrangian multipliers. *Numerische Mathematik*, 20:179–192, 1973.

Belytschko T., Moës N., Usui S., and Parimi C. Arbitrary discontinuities in finite elements. *Int. J. Numer. Meth. Engng*, 50:993–1013, 2001.

Brezzi F. On the existence, uniqueness and approximation of saddle–point problems arising from lagrange multipliers. *RAIRO Anal. Numér.*, 8:129–151, 1974.

Carrica P., Paik K., Hosseini H., and Stern F. Urans analysis of a broaching event in irregular quartering seas. *J. Marine Sci. Technol.*, 13:395–407, 2008.

Fries T.P. and Belytschko T. The intrinsic XFEM: a method for arbitrary discontinuities without additional unknowns. *Int. J. Numer. Meth. Eng.*, 68:1358–1385, 2006.

Ganesan S., Matthies G., and Tobiska L. On spurious velocities in incompressible flow problems with interfaces. *Comput. Methods Appl. Mech. Engrg.*, 196:1193–1202, 2007.

Gross S. and Reusken A. An extended pressure finite element space for two-phase incompressible flows with surface tension. *J. Comput. Phys.*, 224:40–58, 2007a.

Gross S. and Reusken A. Finite element discretization error analysis of a surface tension force in two-phase incompressible flows. *SIAM J. Numer. Anal.*, 45:1679–1700, 2007b.

Leclerc C. and Masson C. Wind turbine performance predictions using a differential actuator–lifting disk model. *J. Solar Energy Engng.*, 127:200–208, 2005.

Meyer C. and Kröger D. Numerical simulation of the flow field in the vicinity of an axial flow fan. *Int. J. Numer. Meth. Fluids*, 36:947–969, 2001.

Minev P.D., Chen T., and Nandakumar K. A finite element technique for multifluid incompressible flow using Eulerian grids. *J. Comput. Phys.*, 187:255–273, 2003.

Reusken A. Analysis of an extended pressure finite element space for two–phase incompressible flows. *Comput. Visual. Sci.*, 11:293–305, 2008.

Tahara Y., Wilson R., Carrica P., and Stern F. Rans simulation of a container ship using a single–phase level–set method with overset grids and the prognosis for extension to a self–propulsion simulator. *J. Marine Sci. Technol.*, 11:209–228, 2006.